

See discussions, stats, and author profiles for this publication at: <https://www.researchgate.net/publication/231696280>

# Hole Nucleation and Growth Induced by Crystallization and Microphase Separation of Thin Semicrystalline Diblock Copolymer Films

ARTICLE *in* MACROMOLECULES · AUGUST 2004

Impact Factor: 5.8 · DOI: 10.1021/ma0357366

---

CITATIONS

14

---

READS

12

8 AUTHORS, INCLUDING:



Jun Fu

Ningbo Institute of Materials Technology and...

74 PUBLICATIONS 1,771 CITATIONS

SEE PROFILE



Jian Li

Agency for Science, Technology and Researc...

32 PUBLICATIONS 648 CITATIONS

SEE PROFILE

# Hole Nucleation and Growth Induced by Crystallization and Microphase Separation of Thin Semicrystalline Diblock Copolymer Films

Jun Fu,<sup>†</sup> Yang Cong,<sup>†</sup> Jian Li,<sup>†</sup> Bin Luan,<sup>‡</sup> Caiyuan Pan,<sup>‡</sup> Yuming Yang,<sup>†</sup> Binyao Li,<sup>†</sup> and Yanchun Han<sup>\*,†</sup>

State Key Laboratory of Polymer Physics and Chemistry, Changchun Institute of Applied Chemistry, Chinese Academy of Sciences, 5625 Renmin Street, Changchun 130022, P. R. China, and Department of Material Science and Engineering, University of Science & Technology of China, Hefei 230026, P. R. China

Received November 19, 2003; Revised Manuscript Received May 18, 2004

**ABSTRACT:** We have investigated the hole nucleation and growth induced by crystallization of thin crystalline-coil diblock copolymer films. Semicrystalline rodlike assemblies from neutral/selective binary solvent are used as seeds to nucleate crystallization at temperatures above the glass transition temperature ( $T_g$ ) but below melting point ( $T_m$ ). The crystallization of nanorods drives neighboring copolymer chains to diffuse into the growing nanorods. Depletion of copolymer chains yields hole nucleation and growth at the edge of the nanorods. Simultaneously, the polymer chains unassociated into the nanorods were oriented by induction from the free surface and the substrate, leading to limitation of the hole depth to the lamellar spacing,  $\sim 20$  nm. The holes, as well as the nanorods, grow as  $t^\alpha$ , where  $t$  is the annealing time and a crossover in the exponent  $\alpha$  is found. The orientation and stretching of the copolymer chains by the surface and interface are believed to accelerate the crystallization, and in turn, the latter accelerates the growth rate of the holes. At  $T > T_m$ , the grains melt and the copolymer chains relax and flow into the first layer of the film.

## Introduction

Block copolymers are composed of covalently bonded sequences of chemically distinct repeat units. The thermodynamic incompatibility of the blocks drives a microphase separation when the homogeneous copolymer melt is cooling down to below the order-disorder transition temperature ( $T_{ODT}$ ), at which the blocks begin to segregate from disordered melt into periodic domains of different blocks.<sup>1–3</sup> The segregation strength<sup>2</sup> is primarily determined by the enthalpy and entropy reasons and usually scaled by  $\chi N$ , the product of the Flory-Huggins parameter ( $\chi$ ) between the blocks and the total degree of polymerization ( $N$ ) of the copolymer. For symmetric diblock copolymers, microphase separation is expected at  $\chi N > 10.5$  according to theoretical prediction.<sup>2</sup> In general, both theoretical and experimental studies have revealed abundant morphologies of segregated block copolymers including body-centered-cubic spheres (BCC), hexagonal cylinders (HEX), gyroid (G), and lamellae (LAM), etc., depending on the volume fraction ( $f$ ) of the block copolymers.<sup>1–3</sup>

Block copolymers at surface and interface are of interest for both theoretical and industrial significance.<sup>1–4</sup> The ordering of block copolymers therein is much different from those in bulk due to the lowering of surface free energy and specific attraction of substrates.<sup>5–7</sup> When annealing thin diblock copolymer films above the glass transition temperature ( $T_g$ ) but below  $T_{ODT}$ , the blocks prefer to segregate to the free surface or substrate due to the specific affinities between the boundaries, leading to orientation of copolymers.<sup>6</sup> Af-

terward, the orientation propagates toward interior.<sup>7–9</sup> Stable films should initially fulfill the quantization constraint in thickness,  $h_i = nL$  or  $h_i = (n + 1/2)L$ , depending on the boundary conditions. Here  $h_i$  is initial film thickness,  $n$  is an integer, and  $L$  is the lamellar period. Otherwise, the films are unstable and the instability will be relaxed in manner of spinodal decomposition (SD)<sup>10</sup> or nucleation and growth (NG).<sup>11,12</sup> The embryonic patterns decay into relief structures, i.e., islands, bicontinuous pattern, or holes, depending on the extent of incommensurability between the initial film thickness and lamellar period.<sup>10–19</sup> At late stage, line tension drives coarsening of islands (holes): the islands (holes) larger than a critical dimension coarsen at the expense of smaller ones.<sup>19</sup> The coarsening kinetics for rarified systems is nearly universally accepted as an asymptotic power law,<sup>15–17</sup>  $\langle R \rangle \propto t^{1/3}$ , where  $\langle R \rangle$  is the average island (hole) diameter and  $t$  is the annealing time. Two-dimensional pressure relaxation due to viscous flow within coherent layers has been theoretically<sup>19</sup> analyzed as one of the possible mechanisms and recently identified experimentally<sup>20</sup> as the rate-determining step due to the prevalent defects at edge of elevations that channel the copolymer flow to the coherent layer for ripening.

The interplay between the crystallization and microphase separation in bulk block copolymers with one crystallizable block has been widely investigated<sup>21–24</sup> and reviewed.<sup>25</sup> The microphase-separated structure provides excellent model systems for investigation of confined crystallization of polymers. The confinement strength is largely determined by the relation between the  $T_{ODT}$ , the glass transition temperature ( $T_g$ ) of amorphous blocks, and the crystallization temperature ( $T_c$ ) of the crystalline blocks.<sup>21,23,24</sup> For  $T_c < T_g < T_{ODT}$ , the crystallization is strictly confined between hard

<sup>†</sup> Chinese Academy of Sciences.

<sup>‡</sup> University of Science & Technology of China.

\* Corresponding author: Fax +86-431-5262126; e-mail ychan@ciac.jl.cn.

walls. On the other hand, for  $T_g < T_c < T_{ODT}$  the crystallization takes place between rubbery surroundings, and thus it would deform the well-established segregated morphology.

Recently, interest has been arising on the confined crystallization of coil-crystalline block copolymer films.<sup>26–30</sup> Their investigations were mainly focused on the problem how crystallization would influence or be affected by oriented film geometry. Reiter et al.,<sup>26</sup> Optiz et al.,<sup>27</sup> and Hong et al.<sup>28</sup> independently studied the PEO crystallization occurred in preoriented PEO-PBh<sup>26,27</sup> and PEO-PBD<sup>28</sup> lamellar films. They found PEO lamellae perpendicular to the substrate at large undercooling and parallel to the substrate in melt. The vertically oriented crystalline stems, according to investigation by Optiz et al.,<sup>27</sup> led to an increase in thickness of lamellar films due to chain stretching of both blocks. The crystallization induced increase in density of PEO blocks, accompanied by contraction in the lateral direction, which resulted in cracking of the film. However, crystallization of PEO blocks confined in microphase-separated parallel multiple PEO layers could be in orientational registry through the 10 nm amorphous layers.<sup>28</sup> Lammertink and co-workers examined the crystallization of films of an asymmetric crystalline-coil polyferrocenyldimethylsilane-*block*-polyisoprene (PFS-*b*-PI).<sup>29</sup> For the films with mixed morphology of holes and wormlike structure, the PFS crystallization took place at room temperature to produce hedritic structures over the whole surface of the films, completely destroying the wormlike morphology. Very recently, Zhang and co-workers<sup>30</sup> found that crystallization preferred to occur at the edge of relief structures of segregated PS-*b*-PCL films since, as they argued, the stretched PCL blocks therein could serve as nucleation agents during polymer crystallization. However, most efforts by far have been devoted to polymer crystallization in microphase-separated relief domains. Less is known about the influence of block crystallization on the relaxation of film instability and the subsequent formation of relief structures. Particularly, for  $T_g < T_c < T_{ODT}$ , it was natural to expect crystallization accompanying the microphase separation of unlike blocks.

In this paper, an approximately symmetric crystalline-coil diblock copolymer, poly(L-lactic acid)-*block*-polystyrene (PLLA-*b*-PS), is used to study the effects of crystallization of PLLA blocks on the surface orientation and film decomposition upon annealing. PLLA blocks at undercooling will crystallize above  $T_g$ 's of both blocks.<sup>31</sup> Simultaneously, surface-induced orientation and microphase separation will occur due to the strong incompatibility of the blocks. The surface morphology evolution upon annealing was observed in situ by hot stage atomic force microscopy (AFM) in tapping mode. The crystallization of PLLA blocks was found to initiate hole nucleation and growth before and after surface orientation of copolymers, which is much different from the well-known SD or NG mechanisms for relaxation of film instability.

## Experiments

**1. Synthesis and Characterization of Block Copolymer.** The diblock copolymer of poly(L-lactic acid) and polystyrene, PLLA-*b*-PS, was synthesized<sup>32</sup> by using successive atom transfer radical polymerization (ATRP) and ring-opening polymerization (ROP). <sup>1</sup>H NMR and gel permeation chromatography (GPC, Waters-150C) gave out the number-average

molecular weight ( $\bar{M}_n = 9400 + 10400$ ) and the molecular weight distribution (MWD)  $< 1.2$ , respectively. At the experimental conditions, the phase segregation strength ( $\chi N$ ) is larger than 10.5.<sup>33</sup>

The glass transition temperatures ( $T_g$ 's) and melting point ( $T_m$ ) were determined with a Perkin-Elmer Diamond differential scanning calorimeter at 10 °C/min. Two glass transitions at 70 and 95 °C and melting at 155 °C were obtained. The melting process onsets at about 145 °C.

**2. Sample Preparation.** We have been able to create loose semicrystalline nanorods by the self-assembly of PLLA-*b*-PS in neutral/selective solvent (THF/CS<sub>2</sub>) mixtures.<sup>34</sup> In particular, CS<sub>2</sub>, a PS-selective solvent,<sup>38</sup> was added drop by drop into 1.0% PLLA-*b*-PS/THF solution with oscillation. Slightly opaque bluish solution was obtained when the CS<sub>2</sub>: THF approximately reached 1:2. Subsequently, the solution was spin-coated onto freshly cleaned polished silicon wafers to produce thin films. The film thickness was determined by ellipsometry as 27 nm.

**3. Atomic Force Microscopy (AFM).** The surface morphology was observed by using a commercial atomic force microscope (SPA300HV/SPI3800N, Seiko Instruments, Inc., Japan). The samples were mounted on a sample stage which is three-dimensionally driven by a piezo tube scanner. Standard gratings were used to calibrate the scanner before use. For tapping mode AFM scan, a silicon cantilever (Olympus, Japan) with an integrated conical tip at the apex worked. The nominal spring constant was 2 N/m, and the resonant frequency was ~70 kHz. The radius of curvature of the tip was about 40 nm, as evaluated by scanning over very sharp needle (radius  $< 10$  nm) array (NT-MDT, Russia).

For in-situ AFM scan, a hot stage integrated to the AFM system is used to change the sample temperature from 20 to 180 °C. The temperature is monitored by a pair of thermal couples which was calibrated by using standard gallium, indium, and tin samples. The accuracy is  $\pm 1$  °C. The morphology evolution was recorded with continuous tapping mode AFM scan at the specific temperatures. Instrumentally, each AFM image is composed of 256 scan lines, and each scan line (e.g., 10  $\mu$ m) is composed of 256 pixels. The scanning rate is 1 Hz, i.e., one line per second. Thus, it takes 256 s to obtain an image. The finishing time is recorded with each image, making it convenient to accurately time the morphology evolution. This is crucial to estimate the film kinetics, as to be detailed in the text.

For positioning the holes or grains in consideration, we position the surface by using the start location, the upper-left point, as the origin, i.e., (0  $\mu$ m, 0  $\mu$ m). Then the upper-right point is (10  $\mu$ m, 0  $\mu$ m) and the bottom-right point is (10  $\mu$ m, 10  $\mu$ m). Any other point in the scan area can be easily positioned. This will help to estimate the surface kinetics below.

## Results and Discussion

**1. Surface Morphology and Evolution below  $T_m$ .** In the THF/CS<sub>2</sub> mixture, the PLLA-*b*-PS diblocks assemble into loose semicrystalline rodlike aggregates.<sup>34</sup> Since the dangling incompletely associated copolymer chains can bridge the assemblies, these nanorods prefer to aggregate into bundles.<sup>34</sup> When spin-coated, these aggregates can be embedded in or supported on the films. It is likely that the aggregates may adopt different conformations, including the so-called flat-on and edge-on. Typical surface morphology is shown in Figure 1. The flat-on semicrystalline aggregates are about 12 nm high and several tens or hundreds of nanometers in width and length. The poor phase contrast (Figure 1c) implies the loose semicrystalline structure. At  $T_g < T < T_m < T_{ODT}$ , the undercooled PLLA blocks will crystallize<sup>31</sup> and the highly incompatible PS and PLLA blocks<sup>33</sup> will segregate simultaneously.



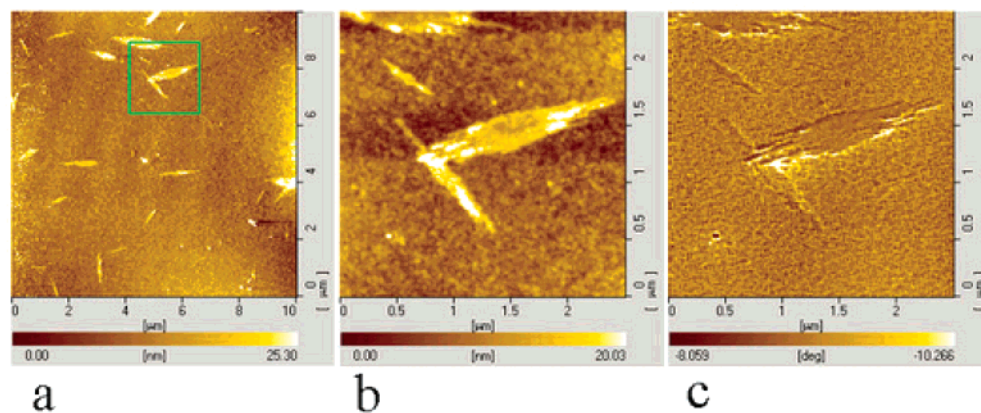


**Figure 1.** Self-assembled bundles of nanorods spin-coated from PLLA-*b*-PS solution in THF/CS<sub>2</sub> mixture. The poor phase contrast in (c) indicates loose semicrystalline structure of the aggregates.

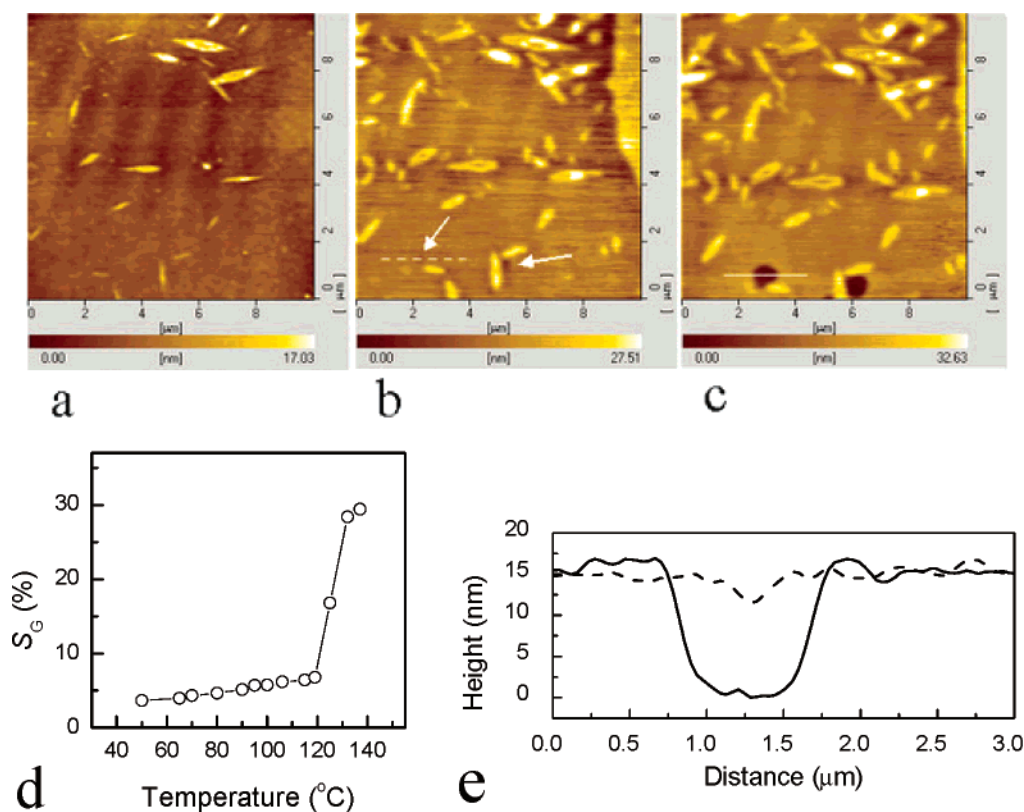


**Figure 2.** Early stage evolution of the film at (a) 95, (b) 125, and (c) 132 °C. (d) Temperature dependence of the fraction of surface area covered by the nanorods or crystalline grains. A sharp increase in grain area is found at 125 °C. (e) Cross-sectional line scan profile along the dash line in (b) and solid line in (c).

When heated well above the  $T_g$ 's (for example 95 °C, Figure 2a), the film became soft and the rods began to slightly grow. Microphase separation and crystallization were not obvious until it reached 125 °C, when an abrupt increase in both the rod size and number was observed (Figure 2b): many tiny granules in the film became larger as new grains. This rapid crystallization was immediately followed by steady process without emergence of new nuclei (e.g., Figure 2c). The lateral evolution of the grains up to 145 °C is summarized in Figure 2d, where the fraction of the surface area covered by the nanorods (grains),  $S_G$ , is plotted as a function of temperature. The remarkable sharp transition at ~125 °C resembles a first-order transition (i.e., crystallization of PLLA blocks<sup>31</sup>).

Significantly, concaves are nucleated at the edge of the grains at  $T \geq 125$  °C (Figure 2b,c). Afterward at

long time annealing or elevated temperature (e.g., 132 °C, Figure 2c), the concaves grew laterally and vertically, according to the cross-section line scan profiles, from ~300 to ~950 nm in diameter and from ~3 to ~15 nm in depth (Figure 2e, dashed and solid lines, respectively).

The isothermal evolution of such grains and holes at 132 °C is in situ traced by hot stage AFM. Typical consecutive AFM images are displayed in Figure 3. At this stage, the grains continued growing, but the grain number kept constant. Meanwhile, new holes were nucleated sporadically but exclusively at the edge of the grains. Normally, the holes are circular at birth but evolved anisotropically into ellipsoids.

The correlation of the hole nucleation to the nanorods and the anisotropic growth are in contrast to the classical hole nucleation and growth in thin films of

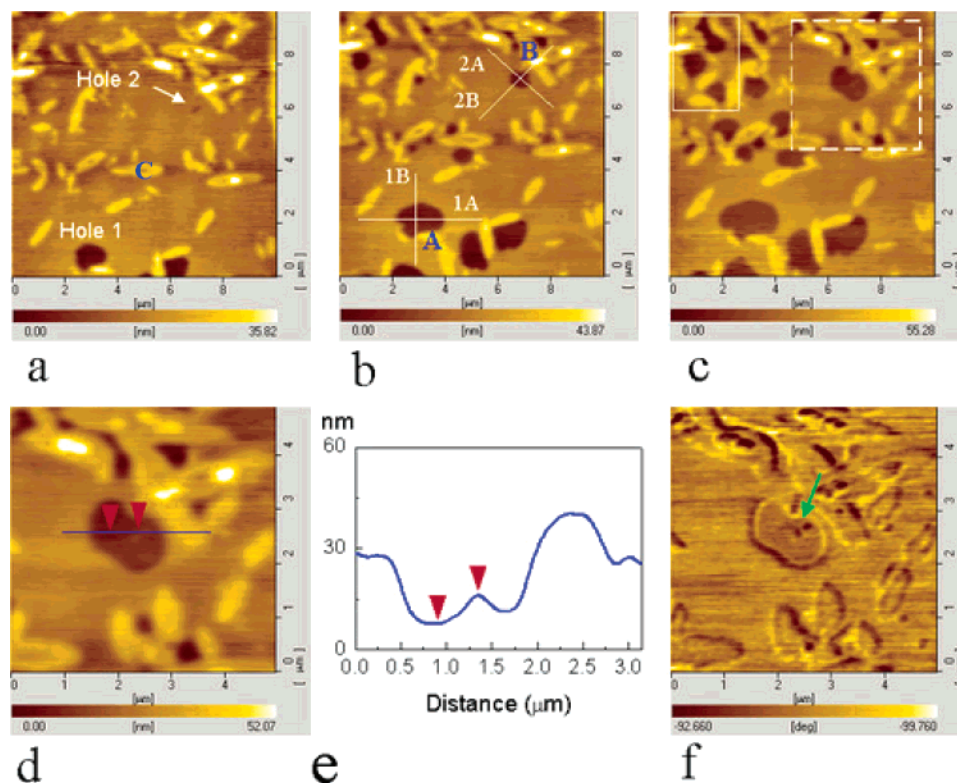


**Figure 3.** Isothermal surface morphology evolution at 132 °C. (a)  $t_0 + 354$  s, (b)  $t_0 + 1119$  s, and (c)  $t_0 + 1887$  s. An area in dashed square in (c) is magnified in (d, height image) and (f, phase image) to specify the crystal stem at the bottom of hole 2. (e) shows the cross-sectional line scan profile along the blue line in (d).

amorphous diblock copolymers.<sup>15–19</sup> More complicated involvement of crystallization, chain diffusion, and microphase separation should be taken into account.

For films free of nuclei, hole nucleation and growth are not observed at  $T < T_m$ . Instead, the films segregate in spinodal decomposition manner (Figure 4). Such SD behavior is not disturbed by integrating isolated nanocrystals in the films (Figure 4b–d).<sup>34</sup> For experiments conducted by far, simultaneous burst of holes was observed only when the films (thinner than 1.5  $L$ ) were annealed at  $T > T_m$  (not shown here).

Therefore, the loose open semicrystalline structure is crucial for the crystallization and hole nucleation in the films. At  $T_g$ 's  $< T < T_m$ , the PLLA blocks crystallize in the assemblies. The incompletely associated copolymer chains may offer channels for mass transport when crystallization induced chain diffusion and folding from outside to inside of the nanorods. That is, the nanorods grew at expense of the neighboring copolymer chains. Thus, holes may emerge once the copolymers were depleted. Since the channels for the chain diffusion are not necessarily identical for different nanorods, the emergence of hole may be sporadic rather than simultaneous.

Remarkably, the nucleation of holes with PLLA crystallization is much different from the SD mechanism and the hole nucleation of metastable films with wrong lamellae.<sup>12</sup> In our case, the phase segregation of the unlike blocks may be accomplished by both crystallization and surface-induced orientation. Thus, the film instability can be relaxed by means other than SD mechanism.

The crystalline grains began to melt at 145 °C, largely at 155 °C and finished at 169 °C (Figure 8). The molten fluid flowed into the holes so that the hole number and area decreased. Finally, only large holes survived. In

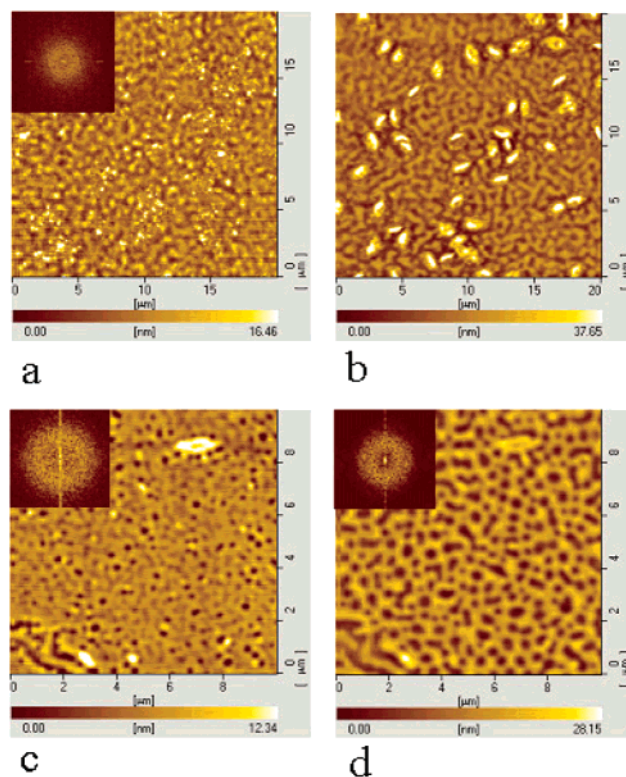


**Figure 4.** Early stage morphology of (a) 36 nm flat film at 107 °C, (b) 57 nm film integrated with isolated crystalline grains at 110 °C, and (c, d) morphology evolution of a 27 nm film integrated with isolated crystal stem on surface at 110 °C. The insets in (a), (c), and (d) are the corresponding 2D FFT patterns.

this process, the Laplace pressure and the line tension work to flatten the film and coarsen the holes. The holes



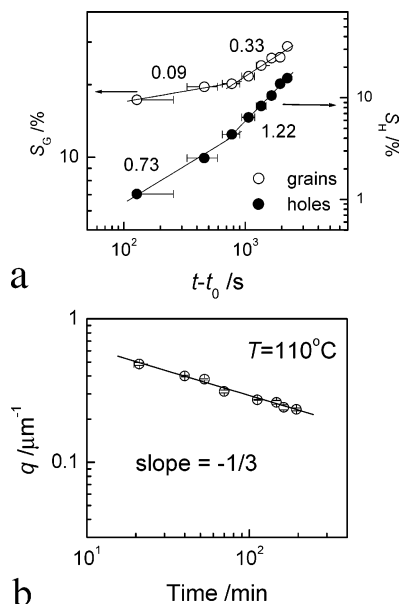


**Figure 5.** Kinetics of (a) the holes and grains drawn from in situ AFM scan at  $132^\circ\text{C}$  and (b)  $-1/3$  power law decay of the wavevector  $q$  at the film surface shown in Figure 4c,d.

became larger and circular at the late stage annealing at  $169^\circ\text{C}$  or higher temperatures. It is remarkable that the hole depth kept constant at  $\sim 20$  nm ( $L$ ) although sometimes they became small due to fluid flow.

**2. Kinetics of the Grains and Holes.** According to the in situ observation of the isothermal morphology evolution at  $132^\circ\text{C}$ , the kinetics of the grains and the holes can be drawn.

First, it is important to choose a proper reference time ( $t_0$ ) to time the process. Since the tapping mode AFM scan started a few seconds after it reached  $132^\circ\text{C}$ , it seems natural to take this start time as  $t_0$ . Thus, the tip went across each of the scan line at  $t_0$ ,  $t_0 + 1$ ,  $t_0 + 2$ , ...,  $t_0 + 255$  s for the first image composed of 256 scan lines (see experimental part). This timing method is rather precise when one only considers the kinetics of individual grain or hole.

However, since the scanning rate is comparable with the surface kinetics, one finds it hard to accurately time the image as a whole. For simplicity, we arbitrarily assume that each image was taken at the half-time for the tip to scan half of the area. Thus, the first image was taken at  $t_0 + 128$  s, and the time for other images can be read from the integrated scanning information. Undoubtedly, a timing uncertainty of  $\pm 128$  s should be kept in mind.

Figure 5a compares the kinetics of the total area fractions of the grains ( $S_G$ ) and the holes ( $S_H$ ) over the scan area. From the linear fittings of the double-logarithm plots, apparent power laws,  $S_i \propto (t - t_0)^\alpha$  ( $i$  denotes the subscripts G and H), are yielded. Acceleration in kinetics is found at  $t - t_0 \approx 775 \pm 128$  s. The exponent values are included in Figure 5a.

Remarkably, the holes grew much faster than the grains. This does not mean violation of mass conservation. Since the film thickness is larger than the thickness of the self-assembled nanorods, the nanorods may likely to exist inside the films, which are invisible for the AFM scan. However, their crystallization will undoubtedly contribute to the nucleation and growth of the holes. An example of such interior nanorods is found in Figure 3c–f, where a bump is evident at the

**Table 1.** Exponents Drawn from Linear Fitting of  $\log D$  vs  $\log t$  Data in Figure 6

		before transition		after transition	
		$\alpha$	SD <sup>a</sup>	$\alpha$	SD <sup>a</sup>
hole 1	$D_{1A}$	0.389	0.004	0.503	0.006
	$D_{1B}$	0.077	0.012	0.381	0.011
	area	0.546	0.028	0.812	0.020
hole 2	$D_{2A}$	0.501	0.035	1.210	0.028
	$D_{2B}$	0.940	0.110	1.290	0.020
	area	1.464	0.079	2.387	0.025

<sup>a</sup> The standard deviations of linear fitting analysis, SD's, are included.

bottom of hole 2. In the phase image (Figure 3f), the bump appeared dark, distinguishing itself as hard material from the surrounding light (soft) materials.<sup>39</sup> This bump did not disappear until it reached  $155^\circ\text{C}$ , indicating that it was PLLA crystals. Similar situations were also found in other samples.

Our grain kinetics obtained by AFM images could not include the kinetics of the grains inside the film and thus cannot represent the total kinetics of all grains that drove the hole nucleation and growth. This is a primary point that we believe should account for the difference between the kinetics of the grains and holes.

In contrast, the microphase separation of thin films undisturbed by crystallization has kinetics of  $q \sim t^{-1/3}$  at  $T < T_m$  (e.g.,  $110^\circ\text{C}$ , Figure 5b), where  $q$  is the surface wavevector drawn from the corresponding two-dimensional fast Fourier transform pattern (Figure 4). This is a typical SD process,<sup>10</sup> without any transition in kinetics at the early stage evolution.

Therefore, the transition in Figure 5a is not inherent behavior of the microphase separation. Neither is such transition similar to the theoretical consideration that predicted transitions of hole (island) coarsening kinetics due to transition between different chain diffusion mechanisms.<sup>16,19</sup> The transition here is unique to such coupled crystallization and microphase separation process.

Therefore, some questions arise. Why should there be a change in the growth of grains and holes at a constant temperature? Since the chain orientation and stretching have been argued to favor crystallization,<sup>30</sup> do such transitions have any correlation to the surface orientation of copolymers?<sup>7–9</sup> The following analysis tries to give rise to possible answers to these questions.

The kinetics of individual holes is considered. Two holes (1 and 2, Figure 3a) are chosen since (1) they neighbored on/to different numbers of grains which we believe directly nucleated and influenced the holes and (2) they could grow without confinement from surrounding grains. (Such confinement can be seen in, for example, the area in the solid rectangle in Figure 3c.)

From Figure 2b,c, the center of hole 1 is located at  $(2.2 \mu\text{m}, 8.6 \mu\text{m})$ . Thus, the tip arrived at the hole center at  $220.4$  s after it reached  $132^\circ\text{C}$ . The following travels of the tip over hole 1 are instrumentally scheduled and recorded and thus could be read conveniently. Since hole 1 had emerged at  $125^\circ\text{C}$  at  $660$  s before it reached  $132^\circ\text{C}$ , hole 1 was born at  $t_0 - 439.6$  s. A similar timing scheme is also used for hole 2 which emerged at  $(7 \mu\text{m}, 3.7 \mu\text{m})$  at the time  $t_0 + 351.4$  s. Also, the tip's travels over hole 2 were instrumentally scheduled and recorded.

Thus, the evolutions of the depth, the lateral dimensions along two directions (A and B, Figure 3b), and the areas of these two holes at  $132^\circ\text{C}$  can be summarized, as displayed in Figure 6.

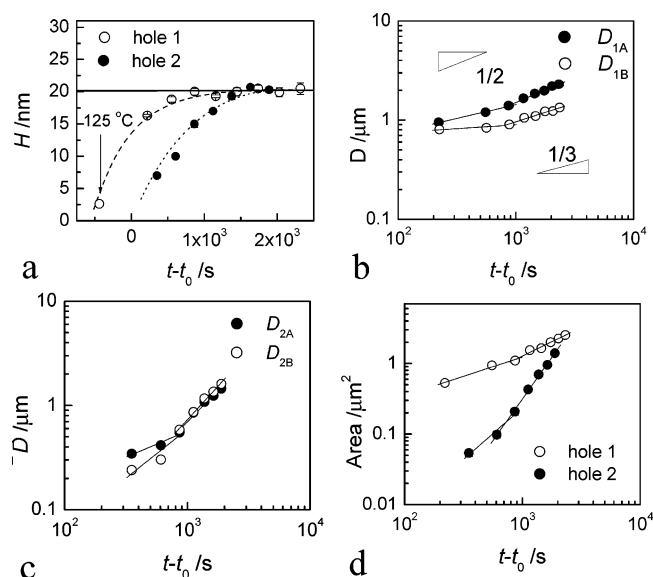


**Figure 6.** Evolution of the hole depth (a), the diameters of hole 1 (b) and hole 2 (c) along directions A and B (see Figure 3b), and the area of these two holes (d) with the annealing time at 132 °C.

In Figure 6a, it is seen that the hole depth progressed asymptotically to  $\sim 20$  nm, or the lamellar period ( $L$ ) of the diblocks.<sup>34</sup> Thereafter, the hole depth kept constant and holes grew laterally only. According to the consecutive AFM images, hole 1 reached a depth of  $L$  between  $t_0 + 552$  s and  $t_0 + 867$  s. This time for hole 2 is between  $t_0 + 1119$  s and  $t_0 + 1375$  s. The limitation of the hole depth to  $L$  indicates the establishment of lamellar structure between  $t_0 + 552$  s and  $t_0 + 867$  s.

The lateral growths of these two holes at 132 °C were also examined. Since the holes progressed anisotropically, their lateral dimensions along the long and short axes (A and B, Figure 3c), as well as the areas, were chosen to access the kinetics of these holes. The data are plotted logarithmically in Figure 6b–d against the logarithm of the annealing time  $\log(t - t_0)$ . Linear fitting yields a power law scaling  $D \sim (t - t_0)^\alpha$ . Acceleration of the kinetics of the holes is also found. The exponents  $\alpha$  drawn from the slopes of the fitting lines are tabulated in Table 1.

The diffusion in block copolymer melts has been investigated by Lodge and co-workers using forced Rayleigh scattering (FRS).<sup>42</sup> The tracer diffusion in disordered copolymer matrix, as well as the copolymer chains, did not behave differently from the homopolymers. However, the tracer diffusion in ordered matrix was largely depressed at the vicinity of the ODT, especially for the diffusion perpendicular to the phase interface.

Significantly in Figures 5a and 6, the transition time of the kinetics of the grains and holes is consistent with the time range when the surface-/interface-induced lamellar structure was established. Therefore, it is natural to expect some correlation between the chain orientation and acceleration of hole and grains kinetics.

It was argued<sup>11</sup> that significant chain stretching should occur at the edge dislocation of the holes or islands because of material transportation or deformation of the interface. Such chain stretching, as recently argued<sup>30</sup> by Zhang and co-workers, could act as nucleation agent during polymer crystallization therein.

In our case, the holes emerged exclusively at the edge of the nanorods (or grains) due to the crystallization-

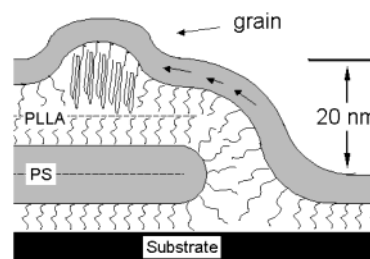


**Figure 7.** Schematics of the hole edge with a grain with crystal stems. The arrows indicate possible fluid flow.

induced chain diffusion and depletion. Once the lamellar structure is established, one then gets a picture that the copolymers crystallize exactly at the edge of the holes where the polymer chains are usually stretched (Figure 7)! According to the arguments in refs 11 and 30, such ordered and stretched chains favor the polymer crystallization. Thus, it may accelerate the copolymer crystallization and, in turn, the (lateral) growth of the holes.

For example, hole 1 was nucleated at stem A (Figure 3b) and the embryonic hole 2 was nucleated by stem B (Figure 3a) inside the film (arrowed in Figure 3f). Remarkably, the lateral growth of stem A is much slower than that of many other flat-on stems (e.g., C in Figure 3a) but very close to the vertical growth of C. This implies that stem A may be an edge-on stem embedded in the film. Thus, the copolymers may diffuse from both sides of stem A into the crystal. In contrast, stem B may attract the surface chains only by its tip. This may account for that hole 1 was nucleated prior to hole 2.

Limited by the time resolution of the relatively slow AFM scan, we failed to follow the very early kinetics of hole 2. From the consecutive images, hole 2 contacted the flat-on crystal stems shortly after its birth. These crystallizing grains would largely drive the hole to expand laterally. Apparently, hole 2 contacted with more grains than hole 1 did, which may account for the rapid growth of hole 2 with respect to that of hole 1.

From Figure 6d and Table 1, the growth of hole 1 was accelerated by a factor of 1.49 while that of hole 2 by a factor of 1.63. This difference may also root from the more diffusion-driving grains that directly induced the growth for hole 2 than for hole 1.

At elevated temperature, e.g., 137 °C, the crystallization-induced hole growth went on until it jumped to 145 °C, the onset temperature of melting (by DSC), when many of the grains began to melt, as shown in Figure 8. The melted block copolymers relaxed and flowed into the first lamellar layer. As a result, many holes dissolved and only large ones survived (Figure 8b). For this viscous fluid, the line tension dominates and drives the initially anisotropic hole circular.<sup>15–19</sup> Thorough melting of the grains and circular holes are obtained at 169 °C (Figure 8c,d). During this process, the hole depth remained constant (20 nm), equal to the lamellar period.

This upon-melting evolution of the holes is displayed in Figure 9. The 0.5 power law growth at 132 °C still holds at 137 °C, followed by a sudden drop in hole diameter at 145 °C. Subsequently, the hole diameter fluctuated from 145 to 155 °C when most of the grains melted. At this stage, the remained grains did not grow any longer. So, the fluctuation in diameter reflects a competition of hole growth driven by line tension and the relaxation of copolymer into the first lamellar layer.

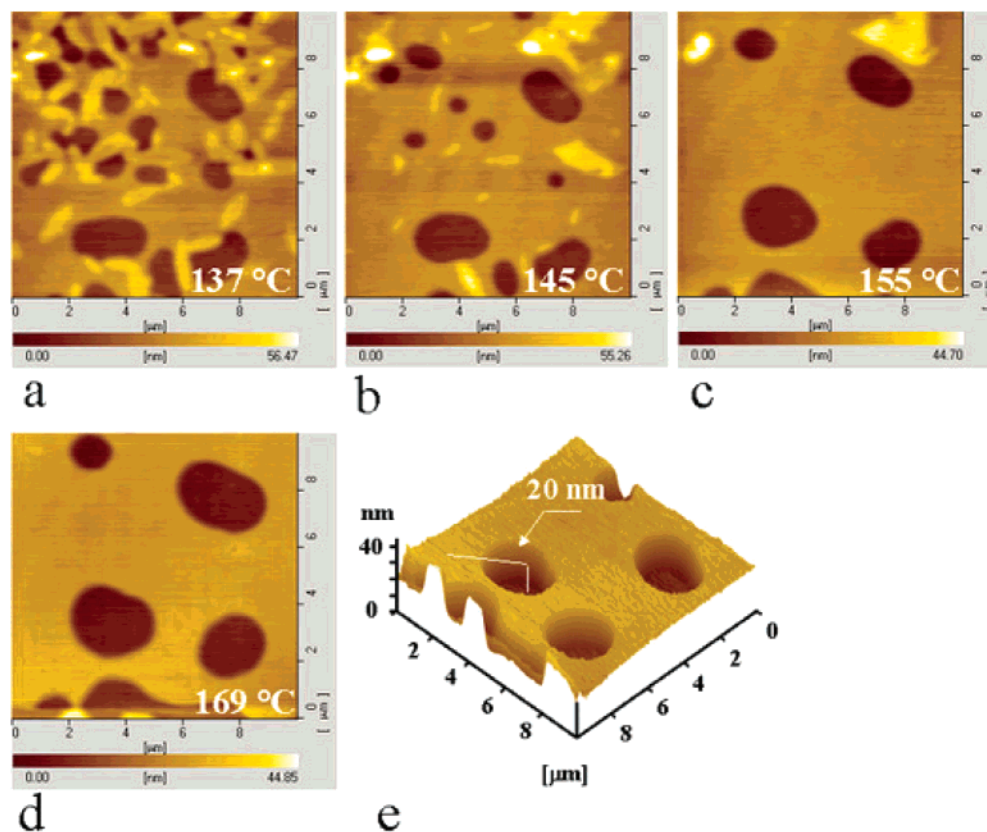


**Figure 8.** Morphology evolution at film surface from 137 °C (a) to 145 °C (b), 155 °C (c), and 169 °C (d). (e) The three-dimensional view of (d). The holes are ~20 nm in height, equal to the lamellar period,  $L$ .

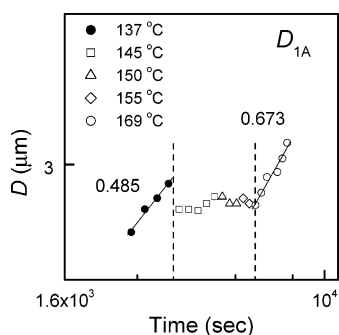


**Figure 9.** Evolution of  $D_{1A}$  from 137 to 169 °C.

When the grains melted, the line tension at hole edge dominates, the coarsening of holes is not different from the widely investigated process of diblock copolymer systems, except that at long time annealing the hole depth slightly increased due to the chain stretching induced by crystallization of PLLA blocks.<sup>26</sup> This is out of the scope of this paper and will not be discussed here.

## Conclusions

Thin films of a crystalline-coil diblock copolymer, PLLA-*b*-PS, integrated with semicrystalline assemblies are created by spin-coating the solutions in mixture of neutral and selective solvents. The loose semicrystalline aggregates are able to crystallize when annealed above  $T_g$  but below  $T_m$ . Upon crystallization, copolymer diffusion from the underlying film to the growing crystalline structures is compelled by crystallization-induced growth of self-assemblies. As a result, holes are nucleated at the edge of grains.

On annealing, surface orientation of the copolymer chains established lamellar structure parallel to the

surface, which limited the vertical development of holes to lamellar period,  $L$ . Laterally, the holes advanced in a manner of power law dependence on annealing time. Within the microphase-separated lamellar structure, the stretched PLLA blocks are ready to enter the crystallizing grains. As a result, the growth of crystallizing grains is accelerated and, in turn, the hole growth is accelerated. The crossovers in Figure 6 demonstrate this effect. Rather than the circular hole (island) geometry driven by line tension, the holes here are ellipsoidal since they grew in an anisotropic way due to the inhomogeneous distribution of the adsorbing grains.

At elevated temperature above  $T_m$ , the crystalline grains melted. The copolymers relaxed and flowed into the underlying surface  $L/2$  layer. At this stage, line tension dominates to make the holes circular and coarsen.

**Acknowledgment.** This work is subsidized by the National Natural Science Foundation of China (50125311, 20334010, 20274050, 50390090, 50373041), the Ministry of Science and Technology of China (2003CB615600, 2002CCAD4000), and the Chinese Academy of Sciences (Distinguished Talents Program, KJXC2-SW-H07, KGXC2-205-03).

## References and Notes

- (1) Bates, F. S.; Fredrickson, G. H. *Annu. Rev. Phys. Chem.* **1990**, *41*, 525.
- (2) Leibler, L. *Macromolecules* **1980**, *13*, 1602.
- (3) Hamley, I. W. *The Physics of Block Copolymers*; Oxford University Press: Oxford, 1998.
- (4) (a) Park, M.; Harrison, C.; Chaikin, P. M.; Register, R. A.; Adamson, D. H. *Science* **1997**, *276*, 1401. (b) Thurn-Albrecht, T.; Schotter, J.; Kästle, G. A.; Emley, N.; Shibauchi, T.; Krusin-Elbaum, L.; Guarini, K.; Black, C. T.; Tuominen, M.



- T.; Russell, T. P. *Science* **2000**, *290*, 2126. (c) Xu, T.; Stevens, J.; Villa, J. A.; Goldbach, J. T.; Guarini, K. W.; Black, C. T.; Hawker, C. J.; Russell, T. P. *Adv. Mater.* **2003**, *13*, 698.
- (5) (a) Fredrickson, G. H. *Macromolecules* **1987**, *20*, 2535. (b) Liu, Y.; Zhao, W.; Zheng, X.; King, A.; Singh, A.; Rafailovich, M. H.; Sokolov, J.; Dai, K. H.; Kramer, E. J.; Schwarz, S. A.; Gebizlioglu, O.; Sinha, S. K. *Macromolecules* **1994**, *27*, 4000. (c) Turner, M. S.; Rubinstein, M.; Marques, C. M. *Macromolecules* **1994**, *27*, 4986. (d) Green, P. F.; Christensen, T. M.; Russell, T. P. *Macromolecules* **1991**, *24*, 252.
- (6) Anastasiadis, S. H.; Russell, T. P.; Satija, S. K.; Majkrzak, C. F. *Phys. Rev. Lett.* **1989**, *62*, 1852.
- (7) (a) Shull, K. R. *Macromolecules* **1992**, *25*, 2122. (b) Menelle, A.; Russell, T. P.; Anastasiadis, S. H.; Satija, S. K.; Majkrzak, C. F. *Phys. Rev. Lett.* **1992**, *68*, 67.
- (8) (a) Russell, T. P.; Coulon, G.; Deline, V. R.; Miller, D. C. *Macromolecules* **1989**, *22*, 4600. (b) Mayes, A. M.; Russell, T. P.; Bassereau, P.; Baker, S. M.; Smith, G. S. *Macromolecules* **1994**, *27*, 749.
- (9) (a) Mansky, P.; Russell, T. P. *Macromolecules* **1995**, *28*, 8092. (b) Morkved, T. L.; Jaeger, H. M. *Europhys. Lett.* **1997**, *40*, 643.
- (10) (a) Joly, S.; Raquois, A.; Paris, F.; Hamdoun, B.; Auvray, L.; Ausserre, D.; Gallot, Y. *Phys. Rev. Lett.* **1996**, *77*, 4394. (b) Maalloum, M.; Ausserre, D.; Chatenay, D.; Gallot, Y. *Phys. Rev. Lett.* **1993**, *70*, 2577.
- (11) Liu, Y.; Rafailovich, M. H.; Sokolov, J.; Schwarz, S. A.; Bahal, S. *Macromolecules* **1996**, *29*, 899.
- (12) Joly, S.; Ausserre, D.; Brotons, G.; Gallot, Y. *Eur. Phys. J. E* **2002**, *8*, 355.
- (13) Green, P. F.; Limary, R. *Adv. Colloid Interface Sci.* **2001**, *94*, 53.
- (14) (a) Coulon, G.; Russell, T. P.; Deline, V. R.; Green, P. F. *Macromolecules* **1989**, *22*, 2581. (b) Maalloum, M.; Ausserre, D.; Chatenay, D.; Coulon, G.; Gallot, Y. *Phys. Rev. Lett.* **1992**, *68*, 1575. (c) Coulon, G.; Daillant, J.; Collin, B.; Benattar, J. J.; Gallot, Y. *Macromolecules* **1993**, *26*, 1582.
- (15) (a) Lifshitz, I. M.; Slyozov, V. V. *J. Phys. Chem. Solids* **1961**, *19*, 35. (b) Marqusee, J. A. *J. Chem. Phys.* **1984**, *81*, 976.
- (16) Nyrkova, I. A.; Semenov, A. N. *Polym Prepr. (Am. Chem. Soc., Polym. Div.)* **1994**, 564.
- (17) (a) Bassereau, P.; Brodbreck, D.; Russell, T. P.; Brown, H. R.; Shull, K. R. *Phys. Rev. Lett.* **1993**, *71*, 1716. (b) Ardell, A. J. *Phys. Rev. Lett.* **1995**, *74*, 4960. (c) Bassereau, P.; Brodbreck, D.; Russell, T. P.; Brown, H. R.; Shull, K. R. *Phys. Rev. Lett.* *74*, 4961.
- (18) Coulon, G.; Collin, B.; Chatenay, D.; Gallot, Y. *J. Phys. II* **1993**, *3*, 697.
- (19) Grim, P. C. M.; Nyrkova, I. A.; Semenov, A. N.; ten Brinke, G.; Hadziioannou, G. *Macromolecules* **1995**, *28*, 7501.
- (20) Heier, J.; Kramer, E. J.; Groenewold, J.; Fredrickson, G. H. *Macromolecules* **2000**, *33*, 6060.
- (21) (a) Loo, Y.-L.; Register, R. A.; Ryan, A. J. *Phys. Rev. Lett.* **2000**, *84*, 4120. (b) Loo, Y.-L.; Register, R. A.; Ryan, A. J. *Macromolecules* **2002**, *35*, 2365. (c) Li, L.; Séréro, Y.; Koch, M. H. J.; de Jeu, W. H. *Macromolecules* **2003**, *36*, 529.
- (22) (a) Hamley, I. W.; Fairclough, J. P. A.; Terrill, N. J.; Ryan, A. J.; Lipic, P. M.; Bates, F. S.; Towns-Andrews, E. *Macromolecules* **1996**, *29*, 8835. (b) Mai, S.-M.; Fairclough, J. P. A.; Viras, K.; Gorry, P. A.; Hamley, I. W.; Ryan, A. J.; Booth, C. *Macromolecules* **1997**, *30*, 8392.
- (23) (a) Zhu, L.; Cheng, S. Z. D.; Calhoun, B. H.; Ge, Q.; Quirk, R. P.; Thomas, E. L.; Hsiao, B. S.; Yeh, F.; Lotz, B. *J. Am. Chem. Soc.* **2000**, *122*, 5957. (b) Zhu, L.; Cheng, S. Z. D.; Calhoun, B. H.; Ge, Q.; Quirk, R. P.; Thomas, E. L.; Hsiao, B. S.; Yeh, F.; Lotz, B. *Macromolecules* **2001**, *34*, 1244.
- (24) (a) Qurim, D. J.; Register, R. A.; Marchand, G. R.; Adamson, D. H. *Macromolecules* **1998**, *31*, 4891. (b) Qurim, D. J.; Register, R. A.; Marchand, G. R.; Ryan, A. J. *Macromolecules* **1997**, *30*, 8338.
- (25) Hamley, I. W. *Adv. Polym. Sci.* **1999**, *148*, 113.
- (26) Reiter, G.; Castelein, G.; Hoerner, P.; Riess, G.; Sommer, J.-U.; Floudas, G. *Eur. Phys. J. E* **2000**, *2*, 319.
- (27) Optiz, R.; Lambrev, D. M.; de Jeu, W. H. *Macromolecules* **2002**, *35*, 6930.
- (28) Hong, S.; MacKnight, W. J.; Russell, T. P.; Gido, S. P. *Macromolecules* **2001**, *34*, 2876.
- (29) Lammerlink, R. G. H.; Hempenius, M. A.; Vansco, G. J. *Langmuir* **2000**, *16*, 6245.
- (30) (a) Zhang, F.; Chen, Y.; Huang, H.; Hu, Z.; He, T. *Langmuir* **2003**, *19*, 5563. (b) Zhang, F.; Huang, H.; Hu, Z.; Chen, Y.; He, T. *Langmuir* **2003**, *19*, 10100.
- (31) Vasanthakumari, R.; Pennings, A. J. *Polymer* **1983**, *24*, 175.
- (32) Tao, L.; Luan, B.; Pan, C. Y. *Polymer* **2003**, *44*, 1013.
- (33) Zalusky, A. S.; Olayo-Valles, R.; Wolf, J. H.; Hillmyer, M. A. *J. Am. Chem. Soc.* **2002**, *124*, 12716.
- (34) Fu, J.; Luan, B.; Yu, X.; Cong, Y.; Li, J.; Pan, C.; Han, Y.; Yang, Y.; Li, B. *Macromolecules* **2004**, *37*, 976.
- (35) (a) Raez, J.; Mannes, I.; Winnik, M. A. *J. Am. Chem. Soc.* **2002**, *124*, 10381. (b) Raez, J.; Mannes, I.; Winnik, M. A. *Langmuir* **2002**, *18*, 7229. (c) Wang, X. S.; Winnik, M. A.; Mannes, I. *Macromolecules* **2002**, *35*, 9146.
- (36) Tsunashima, Y.; Suzuki, S. *J. Phys. Chem. B* **1999**, *103*, 8675.
- (37) Kubies, D.; Rypáček, F.; Kovářová, J.; Lednický, F. *Biomaterials* **2000**, *21*, 529–536.
- (38) Mark, J. E. *Polymer Data Handbook*; Oxford University Press: New York, 1999.
- (39) Magnov, S. N.; Reneker, G. H. *Annu. Rev. Mater. Sci.* **1997**, *27*, 175.
- (40) Müller-Buschbaum, P.; Gutmann, J. S.; Lorenz-Haas, C.; Mahltig, B.; Stamm, M. *Macromolecules* **2001**, *34*, 7463.
- (41) Fredrickson, G. H.; Bates, F. S. *Annu. Rev. Mater. Sci.* **1996**, *26*, 501.
- (42) Dalvi, M. C.; Lodge, T. P. *Macromolecules* **1994**, *27*, 3487.

MA0357366